Journal of Materials Chemistry C

Plenty of Room at the Top: Exploiting Nanowire – Polymer Synergies in Transparent Electrodes for Infrared Imagers

Journal:	*Journal of Materials Chemistry C*
Manuscript ID	TC-ART-02-2025-000581.R1
Article Type:	Paper
Date Submitted by the Author:	14-Apr-2025
Complete List of Authors:	Paul, Shlok; New York University Tandon School of Engineering, Department of Chemical and Biomolecular Engineering Mølnås, Håvard ; New York University Tandon School of Engineering, Department of Chemical and Biomolecular Engineering Farrell, Steven; New York University Tandon School of Engineering, Department of Chemical and Biomolecular Engineering Parashar, Nitika; New York University Tandon School of Engineering, Department of Chemical and Biomolecular Engineering Riedo, Elisa; New York University Tandon School of Engineering, Department of Chemical and Biomolecular Engineering Sahu, Ayaskanta; New York University Tandon School of Engineering, Department of Chemical and Biomolecular Engineering

ARTICLE

Plenty of Room at the Top: Exploiting Nanowire – Polymer Synergies in Transparent Electrodes for Infrared Imagers

Received 00th January 20xx,
Accepted 00th January 20xx

DOI: 10.1039/x0xx00000x

Shlok J. Paul,[†a] Håvard Mølnås,[†a] Steven L. Farrell,[a] Nitika Parashar,[a] Elisa Riedo,[a] and Ayaskanta Sahu*[a]

Infrared (IR) photodetectors are playing an increasingly central role in modern technology, expanding well beyond their niches in military applications to emerging fields like machine vision and consumer electronics. While colloidal quantum dot (cQD) IR detectors in the near-IR (NIR) to short-wave IR (SWIR) now rival conventional bulk materials in laboratory testing, scaling them up to fully integrated IR imagers, particularly in the mid-wave IR (MWIR) remains a challenge. One roadblock is the limited availability of top electrodes with high IR transparency and low sheet resistances. Here we present a silver nanowire (Ag-NW) – polyvinyl alcohol (PVA) composite that simultaneously addresses both issues. The composite delivers over 70% optical transmittance across the NIR, SWIR and MWIR regions with a low sheet resistance ~11 Ω sq.$^{-1}$. We demonstrate its integration as a transmissible top contact in a photodiode achieving detectivities ~2.9 x 10^{11} Jones at 1800 nm, which is comparable to bottom illuminated IR cQD detectors.

Introduction

Infrared (IR) photodetection has historically been used in high-end applications, such as space exploration and for military surveillance purposes, but is becoming increasingly important in today's society through emerging applications in agriculture, medicine, search-and-rescue, machine vision and personal devices.[1–4] Despite their growing importance, detectors made from traditional materials such as mercury cadmium telluride (MCT), indium gallium arsenide (InGaAs), and lead sulfide (PbS) remain expensive or toxic. [5]

In this regard, colloidal quantum dots (cQDs), present a promising alternative to epitaxially grown detectors.[6–9] They possess size-dependent optical properties and are solution-processable allowing for facile detector fabrication and wavelength tuning.[10–13] Additionally, cQD detectors hold potential for elevated temperature operation due to suppressed Auger recombination processes.[14,15] Lastly, their compatibility with flexible substrates opens application avenues beyond the substrate limitations of epitaxial detectors. [16]

The development of IR-active cQD photodetectors and focal plane arrays (FPAs) necessitates at least one IR-transparent electrical contact to allow incident radiation to reach the active absorber layer.[17,18] Beyond transparency, the contact must exhibit appropriate energy band alignment with the photoactive layer, be amenable to facile fabrication processes and maintain stability under the thermal conditions dictated by cQD processing.[18–20]

Transparent conductive oxides (TCOs) have served effectively as electrical contacts in the visible (VIS), near-infrared (NIR) and short-wave infrared (SWIR) ranges, however their performance deteriorates in the extended short-wave infrared (e-SWIR) and mid-wave infrared (MWIR) spectrum. While extremely thin films or doped variants of TCOs can be employed in these spectral ranges, they suffer from increased contact resistance.[21–23] Furthermore, the sputtering process of typical TCOs risks inflicting damage to the underlying device layers [24] and the inherent brittleness of TCOs precludes their application in flexible devices.[25] The use of graphene as a transparent electrode in the SWIR has been reported along with a 97% transparency in the MWIR for CVD deposited single layer graphene, but this approach requires special equipment and is not amenable to high-throughput fabrication.[26–30] Graphene oxide is a solution-processable alternative, however it currently suffers from contact uniformity issues and partial MWIR absorption.[31] Traditionally, thin metal films (~5-10 nm) of gold have been employed with cQD detectors to maintain an acceptable transmittance.[18,32–35] But these contacts risk forming non-continuous films when deposited onto solution processed CQD films with rough surfaces.[3]

[a] *Department of Chemical and Biomolecular Engineering, Tandon School of Engineering, New York University, Brooklyn, New York 11201, United States of America.*
† These authors contributed equally to this manuscript.
Supplementary Information available: [details of any supplementary information available should be included here]. See DOI: 10.1039/x0xx00000x

Silver nanowire (Ag-NW) networks have emerged as promising materials for transparent, flexible and wearable optoelectronic devices due to their high conductivity to transparency ratios, mechanical flexibility and ease of preparation. [36] Since their introduction as transparent electrodes in 2008, Ag-NWs have been widely used in the UV-Vis spectrum. [37–41] Moreover, combining quantum dots with Ag-NWs has enabled the fabrication of easily processable solar cells, photodetectors and patternable LEDs. [42–44] However, bare Ag-NW films, face several challenges including poor substrate adhesion, weak wire to wire bonding, high optical haze and Joule heating degradation. Embedding such films in PVA has been demonstrated as an effective solution to some of the afore-mentioned issues and has been successfully employed in OLEDs, solar cells, thin-film heaters and EMI shields.[45–47] Despite the significant work on Ag-NWs relatively few studies have examined their potential as top contacts in IR photodetectors.[48,49] This may be due to the requirement of low temperature curing processes when working with temperature-sensitive IR cQDs like HgTe. [19,50]

In this report, we present a novel hybrid organic-inorganic composite of Ag-NWs and PVA. It exhibits exceptional optical transparency across both the SWIR and MWIR while maintaining a low sheet resistance (R_{sheet}). Implementing this composite in a prototypical SWIR cQD HgTe photodiode yields device performances comparable to conventional silver metal contacts. Our top-illumination architecture achieves figures of merit similar to state-of-the-art bottom illuminated HgTe photodiodes.[23,51–53] The versatility of this solution-processable, conductive and IR-transparent composite makes it valuable for vertical photodetector architectures and may have a larger impact in the MWIR where availability of transparent electrodes with compatible fabrication processes are currently limited.

Experimental

Chemicals and substrates

Silver nanowires in isopropyl alcohol (Ag-NWs in IPA, 20 mg/mL) were purchased from ACS Material LLC. The nanowires have a length range of 10-30 µm and a diameter of 120 nm. Polyvinyl alcohol (PVA, 99+% hydrolyzed, M_W 85,000-124,000), tellurium (Te, granular, -5-+50 mesh, 99.99%), oleylamine (OlAm, technical grade, 70%), toluene ($C_6H_5CH_3$, anhydrous, 99.8%), 1-dodecanethiol (DDT, ≥98%), chlorobenzene (C_6H_5Cl, anhydrous, 99.8%), dimethyldidodecylammonium bromide (DDAB, 98%), trioctylphosphine (TOP, 97%), ethyl alcohol (EtOH, anhydrous, 200 proof, ≥99.5%), tetrachloroethylene (TCE, anhydrous, ≥99%), hexane (C_6H_{14}, anhydrous, 95%), 1,2-ethanedithiol (EDT, technical grade, ≥90%), hydrochloric acid (HCl, puriss. 24.5-26.0%), 2-propanol (IPA, anhydrous, 99.5%) and oleic acid (OA, 90%) were purchased from Sigma-Aldrich. Acetone (CH_3COCH_3, reagent grade), isopropyl alcohol (C_3H_7OH, reagent grade) and methanol (CH_3OH, reagent grade) were purchased from Greenfield Global Inc. Titanium oxide nanoparticles (TiO_2 NP, BL/SC & T600/SC grade) were purchased from Solaronix SA. Tin (IV) oxide nanoparticles (SnO_2 NP, 15% in aqueous colloidal dispersion) was purchased from Thermo Fisher Scientific Chemicals Inc. Mercury chloride ($HgCl_2$, >99.5%) and silver nitrate ($AgNO_3$, ≥99.0%) were purchased from ACS Reagents. In-house deionized water (DI water) was utilized. All chemicals were used as received without further purification.

0.2 mm thick, 9.5 x 9.5 mm glass substrates were purchased from Thin Film Devices. 0.5 mm thick, 100 mm diameter single-side polished silicon wafers having <100> orientation were purchased from University Wafer and cut into 10 x 10 mm substrates using a Disco DAD 3220 single spindle dicing saw. 1.1 mm thick, 15 x 15 mm glass substrates with 50 nm indium tin oxide (ITO) covering 2/3 of the substrate and 0.55 mm thick, 10 x 10 mm sapphire substrates were purchased from South China Science & Technology Company Ltd. 1.1 mm thick, 20 x 15 mm glass substrates with 100 nm thick ITO interdigitated electrodes (IDE) were purchased from Ossila Ltd. Before use, all substrates were cleaned by sonication in acetone, IPA and methanol (10 minutes in each) followed by 20 min plasma treatment in a PDC-001-HP Benchtop Plasma Cleaner from Harrick Plasma.

Composite film fabrication

PVA was dissolved in DI water (typically 500 mg in 10 mL) under stirring and 115 °C heating overnight to form a ~5 wt% PVA stock solution. Ag-NWs in IPA stock solution was added to the PVA stock solution at different ratios to form 10 wt%, 20 wt% and 30 wt% Ag-NW in PVA solution. Specifically, 250 µL 5 wt% PVA in DI water was used as a base volume and 69 µl, 156 µL or 268 µL Ag-NW in IPA stock solution was added for 10 wt%, 20 wt% and 30 wt% Ag-NW, respectively. The Ag-NW in IPA stock solution was mixed gently by tilting back and forth before extracting the required volume, and the composite solutions were mixed in a similar manner. Vortexing at a low speed was also found to result in effective mixing. More rigorous sonication could not be used due to the fragile nature of the Ag-NWs and the risk of NW breakage.

Ag-NW PVA composite films were deposited onto different substrates through spin coating (static or dynamic dispense, 4000 rpm for 60 sec) under ambient conditions. Thin films were annealed on a hot plate at 40-44 °C for 1 min, followed by vacuum drying in a glovebox antechamber overnight.

Mercury telluride (HgTe) synthesis

Mercury compounds are highly toxic. Handle them with special care.

The synthesis procedure was adapted from Shen et al.[54] In a nitrogen (N_2)-filled glovebox, 54 mg $HgCl_2$ was added to 5 mL degassed OlAm in a glass vial. After stirring at 100 °C for 45 min, $HgCl_2$ was fully dissolved, and the temperature was reduced to 85-90 °C. 0.1 mL 1_M TOP-Te diluted with 5 mL degassed OlAm was injected, and a gradual color change from light yellow to black was observed. After 5 min, additional 0.1 mL 1_M TOP-Te was added. After another 3 min, the reaction was quenched by adding a mix of 1 mL 1-DDT, 2 mL TOP and

5 mL TCE. The solution was transferred to a centrifuge tube and an equal volume of IPA was added, followed by centrifugation at 5000 rpm for 5 min. The supernatant was discarded, and the precipitate was re-suspended in 10 mL chlorobenzene and stored under N_2 until further use.

Before use for dip coating, 1 mL 0.1_M DDAB in IPA and additional EtOH was added until mild turbidity was observed, and the solution was centrifuged at 5000 rpm for 5 min. The supernatant was discarded, and the precipitate was re-suspended in 10 mL toluene.

Silver telluride (Ag_2Te) synthesis

The synthesis procedure was adapted from Shen et al.[54] In a N_2-filled glovebox, 34 mg $AgNO_3$, 4 g OlAm and 0.5 mL OA was added to a glass vial. After stirring at 70 °C for 30 min, the temperature setpoint was increased to 160 °C, and 0.5 mL TOP was injected while the solution temperature was rising. At 160°C, 0.2 mL 1M TOP-Te was injected, and the reaction was allowed to proceed for 10 min, before natural cooling and storage in an explosion-proof refrigerator until needed.

Immediately before use, 1 mL of the stock solution was precipitated with methanol and re-suspended in a mix of 200 µL 1-DDT and 800 µL toluene. The CQDs were precipitated through addition of methanol and centrifugation before resuspension in 1 mL hexane.

Current-voltage curves, shunt, series and sheet resistance

Current-voltage (I-V) and current density-voltage (J-V) curves were established using a Keithley 2400 source measuring unit (SMU) with reported default measurement resolution of 10 pA and a measurement accuracy of ± 0.029 % + 300 pA. The shunt resistance, R_{sh}, was determined as the inverse slope of I-V curves for each photodetector device, scanning from -10 mV to 10 mV. The series resistance, R_S, was determined through fitting to the diode equation, as discussed in Section 6 of the SI. For R_{sheet} measurements, Ag-NW - PVA composite or metallic Ag films were deposited onto cleaned glass substrates as described above. For the composite samples, Ag paste was applied to all four corners of the sample. R_{sheet} was measured using a home-built setup following a standard 4-probe van-der-Pauw method in a N_2-filled glovebox. Specifically, using Keithley 2400 source meters, voltages were measured upon applying currents between alternating pairs of contacts, and average horizontal and vertical resistances were calculated in a custom-made Labview program. R_{sheet} was reported following an iterative numerical calculation solving the van-der-Pauw formula.

UV-Vis spectroscopy

Ag-NW - PVA composite samples were deposited onto clean 1x1 cm glass substrates as described above. HgTe CQDs samples were deposited onto clean sapphire (Al_2O_3) windows from Thorlabs through drop casting followed by swirling. A Cary 5000 UV-Vis-NIR spectrophotometer from Agilent Technologies was used to measure the transmittance or absorbance of the thin-film samples in air at 1 nm interval and 0.1 sec average time. Blank, clean glass and sapphire substrates were used for background correction.

FTIR spectroscopy

Ag-NW - PVA composite samples were deposited onto cleaned sapphire substrates as described above. A Nicolet 6700 FTIR was utilized to record the FTIR spectra of the thin-film samples in air, using a blank, clean sapphire substrate for background correction.

Scanning Electron Microscope (SEM)

Ag-NW - PVA composite samples were deposited onto cleaned silicon substrates as described above. A Merlin (Carl Zeiss) Gemini Ultra-55 Analytical Field Emission Scanning Electron Microscope (FESEM) was used to image the samples at 3 V accelerating voltage and 4 mm working distance. ImageJ software was used to evaluate the image area covered by Ag-NWs.

Atomic Force Microscope (AFM)

Ag-NW - PVA composite samples were deposited onto cleaned glass substrates as described above. A Bruker Dimension Icon Atomic Force Microscope was used in ScanAsyst Air mode to measure film thickness and roughness. In this mode, the gain and frequency used during the measurement is optimized by the software. A thin tweezer was used to scratch the film surface, and the AFM tip was run across the scratch at a resolution of 1024 scans per line. The film thickness was evaluated as the average difference between the height at substrate level and points on the film some distance away from the scratch to avoid ridge effects.

Kelvin Probe Force Microscopy (KPFM)

Ag-NW - PVA composite samples were deposited onto clean 10 x 10 mm gold substrates using the same deposition and preparation protocols above. Work function measurements were performed with the Frequency-Modulated Kelvin Probe Force Microscopy (FM-KPFM) mode on the Bruker Multimode 8 Atomic Force Microscope (AFM) and by using silicon tip on silicon nitride cantilevers with resonance frequency of about 300 kHz and spring constant of about 0.8 N/m (Bruker PFQNE-AL). Silver paste was used to electrically connect the sample with a conductive disc. The topography and contact potential difference (CPD) images (4.5 × 4.5 µm^2, 256 × 256 pixels) were collected at a scan rate of 0.4 Hz. The work function of Ag nanowires was obtained from the CPD images using the following equation: $W_F^{Ag\ nanowire} = W_F^{tip} + e.CPD$; where e is the charge of an electron and W_F^{tip} is the work function of the tip. W_F^{tip} (= 4.68 eV) was measured by performing FM-KPFM on gold calibration sample (Bruker PFKPFM-SMPL, W_F^{gold} = 5.1 eV).[55] CPD of any given sample was obtained from cross-section line profiles of 30-pixel thickness across the sample.

Thermogravimetric Analysis (TGA)

300 µL Ag-NW stock solution or 250 µL 20 wt% Ag-NW in PVA mixed solution were dried in a clean, tared 80 µL platinum (Pt) pan at 85 - 122 °C for 20 min. Alternatively ~8 mg untreated PVA or ~0.08-0.15 mg spin coated and annealed 20 wt% Ag-NW in PVA film was placed dry in the Pt pan. The thermal response of the samples in the temperature range 25 - 600 °C was evaluated using a TGA550 Thermogravimetric Analyzer from TA Instruments with TRIOS software Version 5.4.0.300. Ramp rates were controlled between 10-20 °C min^{-1}, and 10 min isothermal holds were performed at 110 °C, 300-350 °C, and 600°C.

Device fabrication

A planar TiO_2 NP electron transport layer (ETL) was deposited onto cleaned S162 ITO IDE substrates from Ossila Ltd through spin coating (5000 rpm for 45 sec) of TiO_2 NP BL/SC stock solution in alcohols/water/organic binders in air. Polyimide (Kapton) tape was used to mask the contact pads during this process but was removed prior to annealing of the substrates on a hot plate at 550 °C for 1 h. The photoactive HgTe CQD layer was deposited via dip coating using a custom-built dip coater. Pairs of substrates were dipped sequentially into three beakers at different rates - solution concentrations and number of repetitions listed in **Table S2** in the Supporting Information (SI). The first beaker contained the HgTe CQDs dispersed in toluene, the second beaker contained a mixture of EDT/HCl/IPA to facilitate the ligand exchange, and the third beaker contained neat IPA to wash off excess ligands. A q-tip was used to wipe off the HgTe CQDs from the contact pads and other unwanted areas of the substrate.

The substrates were then masked using polyimide tape, creating a 1-2 mm wide exposed strip perpendicular to the ITO electrodes, as illustrated in **Figure S12** in the SI. The exact width of the exposed strip was determined using a vernier caliper. A 15 nm MoO_3 hole transport layer (HTL) was deposited onto the exposed areas through thermal evaporation in a N_2-filled glovebox. Finally, Ag-NW-PVA composite films with 20 wt% theoretical Ag-NW content were deposited through spin coating under ambient conditions onto one of the substrates from each pair. Static dispense was utilized, and the pipette tip was used to spread the composite ink over the desired area. The sample was then spun at 4000 rpm for 60 sec, followed by annealing on a hot plate at 40-44 °C for 1 min and vacuum drying in a glovebox antechamber overnight.

The twin sample from each pair received the corresponding top contact under investigation; either 100 nm thermally evaporated Ag top electrode, Ag-NW mesh spin coated (static dispense, 2000 rpm for 30 sec) from ~4 mg mL^{-1} Ag-NW dispersion in IPA, or sequential deposition of Ag-NW mesh (deposited as above) and PVA through spin coating 5% PVA in DI water (static dispense, 4000 rpm for 1 min) followed by annealing as for the composite sample.

For samples with SnO_2 NP ETL instead of TiO_2, a commercially available SnO_2 NP dispersion (15 wt% in aqueous solution) was diluted 1:6 in DI water and sonicated for 20 min before filtering using a 0.22 µm syringe filter to ensure an agglomerate-free dispersion. The SnO_2 NPs were then spin coated onto the substrate (dynamic dispense, 3500 rpm for 35 sec), and annealed in air at 170 °C for 45 min.

For samples with Ag_2Te HTL instead of MoO_3, Ag_2Te CQDs in hexane dispersion was spin coated at 2000 rpm for 30 sec, before soaking the substrate in 0.01_M $HgCl_2$ in methanol for 10 sec, methanol rinse and drying in air, followed by 10 sec soaking in 1 vol% EDT/HCl in IPA, IPA rinse and drying in air. This process was repeated twice before application of the top contact as described above.

Photoresponse measurements

The sample photoresponse was characterized using a custom fabricated visible-to-SWIR photoconductivity setup. 300 - 3800 nm broadband light from an incoherent 250 W Oriel Newport Light source equipped with a halogen bulb was collimated, filtered for second order light and chopped at 25 Hz before being focused onto the input slit of a Cornerstone 260 Vis-NIR extended range ¼ m monochromator. Based on the selected monochromator wavelength, suitable high pass filters (375, 715 or 1400 nm) were automatically selected. Maximum power output from the monochromator, while maintaining 39 nm resolution, was ensured through adjusting input and output slits to 3 mm. After collimation, the electromagnetic radiation exiting the monochromator was refocused onto the sample mounted in a dark enclosure. An 843-R-USB power meter coupled with a germanium (Ge) reference detector (818-ST2-IR) was utilized to quantify the wavelength-dependent input power hitting the sample. The generated photocurrent was amplified and converted to a voltage output through a Stanford Research Systems SR570 current preamplifier connected in series with a SR810 lock-in amplifier, allowing for extraction of the photovoltage signal from the light-exposed sample. No applied bias was necessary as these samples had a built-in bias enabling extraction of photogenerated carriers. Sample photovoltage and phase output from the lock-in amplifier were read and saved using a custom-built LabView program. The preamplifier sensitivity setpoint enabled manual back-conversion of photovoltage to photocurrent for further photoresponse evaluation.

Response Time Measurement

To measure the response time of the photodiode, a Thorlabs DC2200 LED driver along with a 970 nm M970L4 LED was used. The sample and LED were placed in an enclosed dark box a set distance apart. The incident power was measured using a Newport 843-R-USB power meter. The sample was connected to a DLCPA-200 low noise amplifier, with no applied bias, whose output was sent to a Tektronix TDS 784C oscilloscope. Utilizing the DC2200 enabled pulsing of the LED while the detector output was measured on the oscilloscope, the rise and fall times were obtained by measuring the time taken to

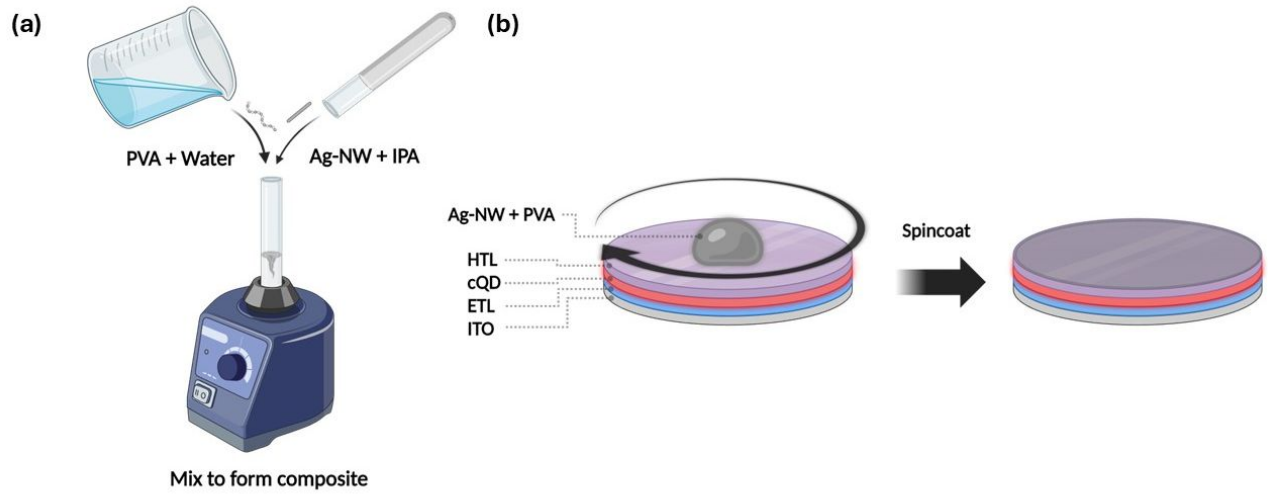

Figure 1. Schematic of fabrication and processing of Ag-NW PVA composite films. (a) PVA in water and Ag-NW in IPA are gently vortexed to form a mixture. (b) The Ag-NW PVA mixture can be spin-cast on top of typical photodiode devices and used as an IR-transparent top electrode. ETL and HTL represent Electron and Hole Transport Layers respectively.

reach between 10% and 90% of the response, respectively. The slight delay observed in LED on vs device on is a result of differing cable lengths from the LED output and the device output to the oscilloscope.

Noise measurements

Noise current spectral density was measured using an SR770 FFT Spectrum Analyzer. The samples were placed in an electromagnetically shielded dark box, and the signal was amplified through an SR570 current preamplifier at 10^{-8} A V^{-1} sensitivity setpoint in low noise and battery mode. A 12 dB oct^{-1} low-pass filter at 1 kHz was employed, and 100 times exponential averaging was activated for the output data. The noise value at 25 Hz at 0 V applied bias was used to calculate the specific detectivity, *D**.

Results and Discussion

Ag-NW - PVA composite films were fabricated as described in the Experimental Section. Briefly, Ag-NWs dispersed in IPA (20 mg mL^{-1}) were mixed with PVA dissolved in DI water (~5 wt%) at specific ratios, and the mixed solutions were spin coated onto photodiode style devices, as illustrated in **Figure 1.** TGA measurements shown in **Figure S1** in the SI demonstrate that the theoretical Ag-NW loading likely is an underestimation of the true Ag-NW content of the films. The films based on 20 wt% Ag-NW – PVA mixed solution contained approximately 50wt% Ag-NWs, likely due to density differences in the colloidal solution during spin coating. However, since the main control parameter during fabrication was the Ag-NW-PVA mixing ratio, the theoretical Ag-NW loading is used throughout the manuscript when comparing the different films.

Optical and electrical properties

Figure 2 shows SEM micrographs of Ag-NW-PVA composite films on silicon with different theoretical Ag-NW loading (10 - 30 wt%). The Ag-NWs, supplied as diameter Ø120 nm and length 30-50 µm, can be observed as dark wire structures embedded in the lighter PVA matrix. Conductive pathways are formed even at 10% loading (Figure 2a), and the interconnectivity increases significantly with increasing loading (Figure 2b-c). Yet, significant areas are left uncovered by NWs (>50% based on analysis of 2D segments in ImageJ, shown in **Figure S2** in the SI), enabling high transmittance of electromagnetic radiation. Figure 2d) shows a close-up of the intersection of two Ag-NWs.

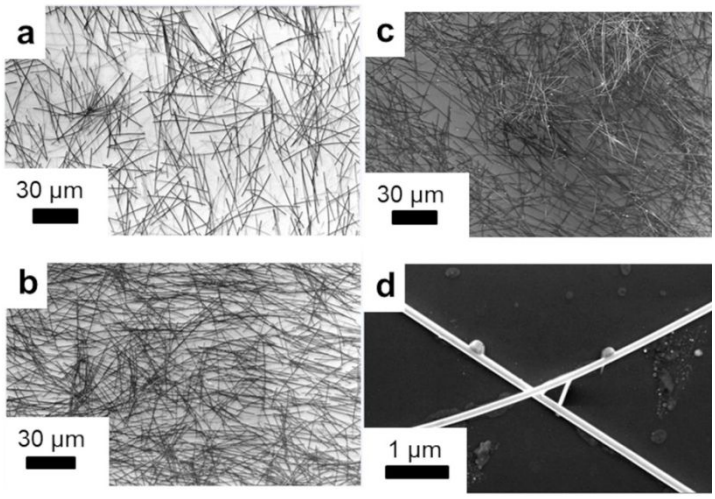

Figure 2. SEM images of Ag-NW-PVA composite films with (a) 10 wt%, (b) 20 wt% and (c) 30 wt% Ag-NWs with cross sectional coverages of 20%, 40% and 49% respectively. (d) Close up of Ag-NW intersection.

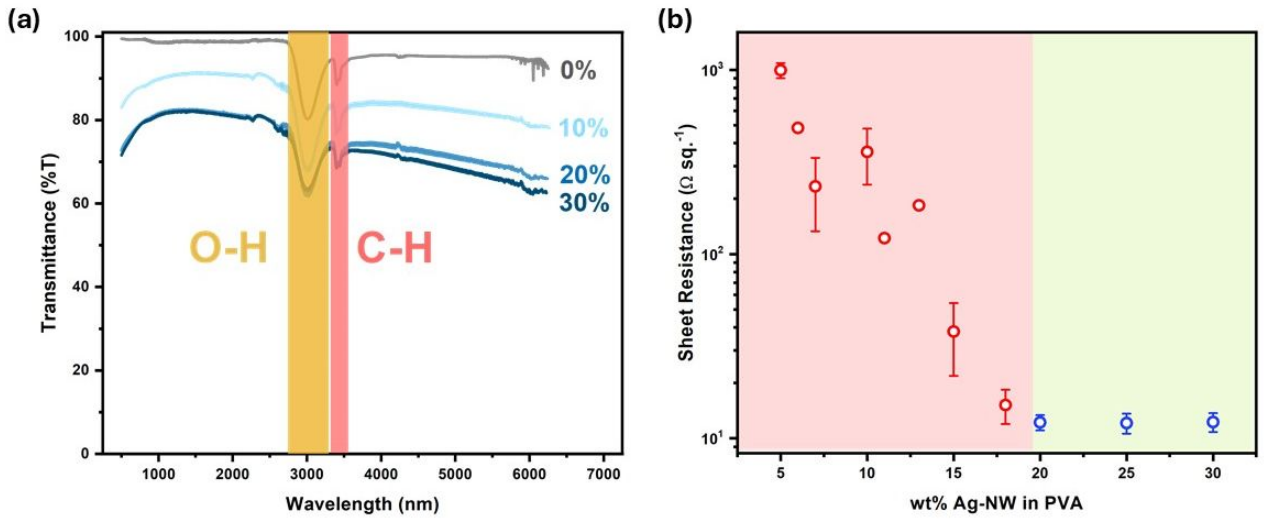

Figure 3. (a) Optical transmittance and (b) electrical sheet resistance for Ag-NW - PVA composite films with different Ag-NW content. In (a) the orange and pink regions represent the absorption from O-H and C-H stretches respectively. In (b) Two distinct regions are observed, one below 20% Ag-NW concentration, where there is high sheet resistance with large scatter marked in red and a green region above the critical concentration showing stable and consistently low sheet resistance.

Figure 3 (a) shows transmittance results for Ag-NW - PVA composite films with different theoretical Ag-NW content. Our composite films show high transmittance (>70%) from the NIR (0.7-1.4 µm), through the SWIR (1.4 - 3 µm) and >60% transmittance into the MWIR range (3-5 µm). Reduced transmittance at ~500 nm is due to the absorption in the Ag-NWs, while reduced transmittance at ~3000-3500 nm is due to the C-H and O-H stretch in the PVA. Additional transmittance data is shown in **Figure S3 and S4** in the SI. Compared to traditional IR photodetector contacts like ITO and FTO,[56,57] having a MWIR transmittance of <50%,[22,58] our films show higher transmittance beyond 3 µm. The trend in transmittance shows dependence on theoretical Ag-NW loading, as expected based on previous reports [45] and SEM images in **Figure 2**. However, while SEM images mainly enable visualization in 2D, the film transmittance is a 3D-effect influenced by achieved film thickness. In accordance with Atomic Force Microscopy (AFM) data shown in **Figure S5-S7** in the SI, the average film thicknesses were determined to 349, 144 and 57 nm for 10%, 20% and 30% theoretical Ag-NW loading, respectively. Utilizing identical spin coating parameters for all three Ag-NW concentrations, the film thickness is mainly a result of the different viscosities of the mixed solutions. Since the film with the lowest theoretical Ag-NW loading also has the largest average thickness, the Ag-NW concentration per vertical cross section is significantly smaller at 10% than at 20% and 30% theoretical loading, substantiating the notable difference in transmittance.

Figure 3 (b) shows the R_{sheet} of Ag-NW - PVA composite films with theoretical Ag-NW loading in the range 5 - 30%. Additional data and statistical considerations are shown in **Figure S8** and **Table S1** in the SI. It can be observed that the R_{sheet} decays with increasing Ag-NW loading and stabilizes around ~11 Ω sq.$^{-1}$ above 15% Ag-NW. This is comparable to other Ag-NW-PVA reports in the literature. [37,45,47,59,60] The stabilization of R_{sheet} at higher loading indicates that a stable conductive network of Ag-NW junctions has been established,[59] as visualized in Figure 2d). Beyond a composition of 20 wt% Ag-NWs, the change in R_{sheet} is negligible while the transmission decreases and hence, we stick with the 20 wt% Ag-NW samples for most of our device fabrication as will be discussed later.

The Ag-NW-PVA films show comparable optical and electrical performance to traditional TCE materials, ITO and FTO, as discussed in Section 5 of the SI in **Figure S9**. Moreover, the R_{sheet} of 20 nm and 100 nm Ag thin films thermally deposited onto 1x1 cm glass substrates were determined to 28.5 Ω sq.$^{-1}$ and 0.4 Ω sq.$^{-1}$, respectively, through the 4-probe van-der-Pauw method. Kelvin Probe Force Microscopy was performed to determine the work function of the Ag-NW-PVA composite with a value of ~4.6 eV as shown in **Figure S10**. Notably this value is comparable to that of Silver and ITO at 4.7 eV facilitating seamless integration into current cQD photodiode stacks. [61,62]

Performance as top contact in an IR photodetector

Vertical photodetectors incorporating Ag-NW-PVA as a top contact were fabricated as described in the Experimental section and in **Figure S11** and **Table S2** in Section 6 of the SI. As a proof of concept, we utilized HgTe cQDs as the photoactive material since these are amongst the best-in-class IR cQDs and the most likely to be used in the SWIR and MWIR ranges. The band diagrams of the devices reported below are drawn in **Figure S12** of the SI.

Figure 4 compares the device architecture and specific responsivity of vertical HgTe cQD photodetectors with Ag-NW - PVA composite top contacts with a twin sample having 100 nm thermally evaporated Ag top contact. These samples were characterized at room temperature in ambient at 25 Hz chopping frequency with 0 V

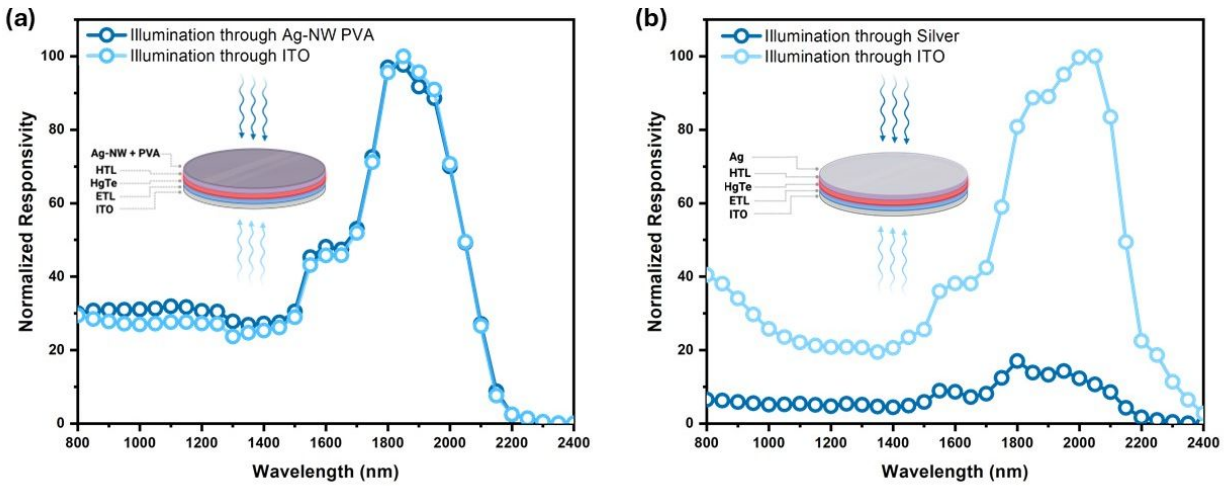

Figure 4. Comparison of the responsivity when illuminated from the top and bottom for (a) Ag-NW top contact devices and (b) Ag top contact devices. Shining through Ag leads to optical loses relative to ITO not seen in the Ag-NW PVA devices.

applied bias. 20 wt% theoretical Ag-NW loading of the composite top contact was chosen based on its favorable reproducibility and high optical transparency described above.

As shown in **Figure 4 (a)**, the devices with Ag-NW - PVA top contacts demonstrate similar photoresponse when illuminated either through the top contact or through the transparent bottom ITO substrate. These results confirm that the Ag-NW PVA top electrode is as transparent as the ITO. Meanwhile the control device in **Figure 4 (b)** shows a marked difference in responsivity when illuminated through the substrate vs through the silver film which is not highly transparent. The devices with Ag-NW PVA top contact in fact show higher responsivity when illuminated through the top as compared to the 100 nm Ag device illuminated through the bottom as shown in **Figure S13**. These results indicate that the Ag-NW-PVA top contact does not limit the performance of conventional cQD based IR detectors, which is important, as it points to direct transferability to optimized cQD based vertical photodetector systems and imagers requiring a top contact with low R_{sheet} and high transmittance from the visible to the MWIR.

In **Figure S14** in the SI, the photoresponse of a set of twin samples comparing 20 wt% Ag-NW PVA composite top contact with Ag-NW mesh top contact is reported as a control experiment. R_{Sh} was 1.7 MΩ and 0.4 MΩ for the devices with mesh and composite top contact, respectively. Devices with 20 wt% Ag-NW PVA composite top contact perform about two orders of magnitude better in terms of responsivity than identical devices with Ag-NW mesh top contact. This demonstrates the benefit of embedding the Ag-NWs in the polymer, improving adhesion, mechanical and electrical stability of the electrode rather than using the NWs in isolation.[46]

A previous report using Ag-NW-PVA composite as a top contact for solar cells fabricated the conductive film through a sequential deposition process where Ag-NWs were deposited onto a glass substrate, followed by PVA, before flipping and gluing the film to polyethylene terephtalate (PET) using a UV sensitive binder.[60] This multistep process results in a localization of the Ag-NWs to one side of the polymer film and thus a lower degree of spatial distribution (of the Ag-NWs), likely decreasing the transmittance of the top contact and effectively the photoresponse of the photodetector. **Figure S15**

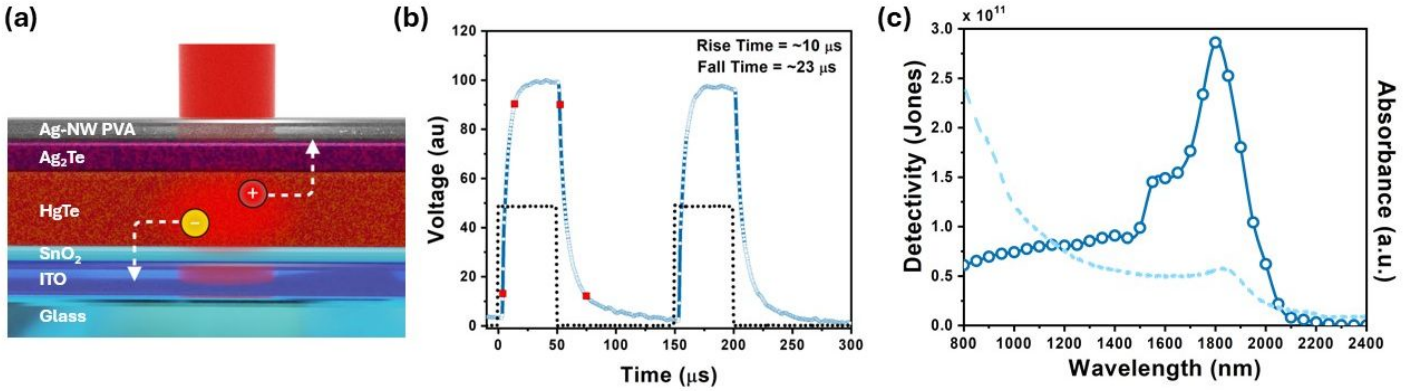

Figure 5. (a) Render of device with FTO/SnO_2/HgTe/Ag_2Te/20% Ag-NW PVA composite with topside illumination. (b) Device time response (Blue curve) under 970 nm illumination (black dotted line) showing rise and fall times of 10 µs and 23 µs. (c) Detectivity (dark blue) and Absorbance (dashed light blue) vs wavelength of the diode with peak D* ~2.9 x 10^{11} Jones at 1800 nm.

in the SI shows the photoresponse of a set of twin samples comparing mixed and sequential deposition of the Ag-NW-PVA composite. R_{Sh} was comparable: 6 MΩ for the devices based on mixed deposition of the top contact and 4.6 MΩ for the devices based on sequential deposition. The devices with top contact deposited from a mixed solution demonstrated up to ~2 times higher responsivity compared to devices with top contact deposited sequentially. This demonstrates the benefit of the spatial distribution of the Ag-NWs in the polymer layer and hence the composite approach.

To push the performance of these SWIR devices further, we employed a Ag_2Te CQD HTL instead of MoO_3 and a SnO_2 ETL instead of TiO_2. The device geometry is shown in **Figure 5 (a).**[57] Current density – voltage (J-V) curves demonstrate diodic behavior, shown in **Figure S16** and **Table S3** in the SI, with a leakage current of ~85 μA cm^{-2} at 0.1 V reverse bias.

The response time of the detector is a useful metric for demonstrating its use in high-speed applications such as IR imaging. A slow response time cannot faithfully reproduce rapid changes in light intensity leading to a smearing of the optical image.[64] We measure the rise and fall time of our diode using a pulsed 970 nm LED and obtain a rise and fall time of 10 μs and 23 μs, respectively **Figure 5 (b)**. Another useful metric is the specific detectivity (*D**) of a photodetector. This parameter indicates how effectively the device can detect low-intensity light signals relative to the inherent noise.[64,65] Here *D** is calculated as a function of wavelength based on Equation 1:[64,66]

$$D^*(\lambda) = \frac{R(\lambda)\sqrt{A}}{\sqrt{I_n^2}} = \frac{i_{ph}(\lambda)}{P_{in}(\lambda)} x \frac{\sqrt{A}}{\sqrt{I_n^2}} \quad (1)$$

where *R(λ)* is the responsivity as a function of wavelength, i_{ph} is the wavelength-dependent photocurrent, P_{in} is the input power to the sample at a certain wavelength, *A* is the device area and I_n is the noise current spectral density. With this device, we were able to achieve a peak *D** of ~2.9 x 10^{11} Jones and a responsivity ~36.5 mA W^{-1} at 1800 nm and 140 Hz under 0V applied bias. Responsivity and noise current density for this device is included in **Figure S17** in the SI. Our *D** and response times are on the same order of magnitude as some of the best performing SWIR HgTe CQD Photodiodes at 300K. A list of reported devices is included in **Table S4** for comparison.

Conclusions

Here we demonstrate that an Ag-NW PVA composite can form robust, solution-processable top contacts that provide high transmittance (>70%) from the visible through the MWIR and offer tuneable sheet resistances down to ~11 Ω $sq.^{-1}$. These composites can be fabricated at room temperature with minimal post-processing making them compatible with temperature-sensitive substrates and cQDs. Using a model HgTe CQD SWIR photodiode system, we demonstrate photodetector performance comparable with conventional evaporated metal top contacts. Our approach of using Ag-NW PVA composites as top contacts can be easily translated to other IR cQD systems and act as an alternative to metal electrodes. Furthermore as syntheses of HgTe and other emerging IR cQDs including device geometries continue to improve, these new systems can potentially benefit from leveraging this transparent top contact for affordable IR detectors.[51,53,67] This study highlights the transformative potential of Ag-NW PVA composites in next-generation IR imaging.

Author contributions

S.J.P.: Investigation, Formal analysis, Visualization, Resources, Data Curation, Writing – original draft, Writing - review & editing. H.M.: Investigation, Formal analysis, Visualization, Resources, Data Curation, Writing – original draft, Writing – review and editing. S.L.F.: Visualization, Writing - review & editing. N.P.: Investigation., Writing – review & editing. E.R.: Methodology, Supervision, Writing – review & editing. A.S.: Conceptualization, Project administration, Funding acquisition, Supervision, Methodology, Validation, Writing – review & editing.

Conflicts of interest

The authors declare the following competing financial interest(s): A.S., H.M. and S.J.P. have filed a patent application 18/804,273 on August 14th, 2024, based on the results of this manuscript.

Data availability

Additional data supporting this article have been included as part of the Supplementary Information. Further data from the main text and supplementary information are provided on the open science framework platform at the link: https://osf.io/ye2as/?view_only=48621a03661b4abfb502ed3fd5bf2d92

Acknowledgements

This study was funded by the Young Faculty Award program of the Defense Advanced Research Projects Agency (DARPA) under the grant D21AP10118. The views, opinions, and/or findings expressed are those of the authors and should not be interpreted as representing the official views or policies of the Department of Defense or the U.S. Government. This work was supported by the Office of Naval Research Grants N00014-20-1-2231 and N00014-24-1-2683. We also gratefully acknowledge support for instrument use, scientific and technical assistance from the NYU Shared Instrumentation Facility through the Materials Research Science and Engineering Center (MRSEC) and MRI programs of the National Science Foundation under

Award numbers DMR-1420073 and DMR-0923251. The work by NP was supported by the US Army Research Office under Awards W911NF2020116. Some figures are created using https://BioRender.com.

Notes and references

1 S. Bianconi and H. Mohseni, *Rep Prog Phys*, 2020, **83**, 044101.
2 H. Lu, G. M. Carroll, N. R. Neale and M. C. Beard, *ACS Nano*, 2019, **13**, 939.
3 T. Nakotte, S. G. Munyan, J. W. Murphy, S. A. Hawks, S. Kang, J. Han and A. M. Hiszpanski, *J. Mater. Chem. C*, 2022, **10**, 790.
4 W. Gong, P. Wang, D. Dai, Z. Liu, L. Zheng and Y. Zhang, *J. Mater. Chem. C*, 2021, **9**, 2994.
5 P. Guyot-Sionnest, M. M. Ackerman and X. Tang, *J. Chem. Phys*, 2019, **151**, 060901.
6 A. Mukherjee, H. Kannan, L. T. Triet Ho, Z. Han, J. Stavro, A. Howansky, N. Nooman, K. Kisslinger, S. Léveillé, O. Kizilkaya, X. Liu, H. Mølnås, S. J. Paul, D. H. Sung, E. Riedo, A. Rumaiz, D. Vasileska, W. Zhao, A. Sahu and A. H. Goldan, *ACS Photonics*, 2023, **10**, 134–146.
7 H. Mølnås, A. Mukherjee, H. Kannan, Z. Han, V. K. Ravi, S. J. Paul, A. K. Rumaiz, W. Zhao, A. H. Goldan and A. Sahu, *Advanced Functional Materials*, 2024, **34**, 2315304.
8 A. Rogalski, M. Kopytko, W. Hu and P. Martyniuk, *Sensors*, 2023, **23**, 7564.
9 A. Rogalski, W. Hu, F. Wang and P. Martyniuk, *Materials (Basel)*, 2024, **17**, 4522.
10 F. P. García de Arquer, D. V. Talapin, V. I. Klimov, Y. Arakawa, M. Bayer and E. H. Sargent, *Science*, 2021, **373**, eaaz8541.
11 F. P. G. Arquer, A. Armin, P. Meredith and E. H. Sargent, *Nat. Rev. Mater*, 2017, **2**, 16100.
12 Origin of Intraband Optical Transitions in Ag2Se Colloidal Quantum Dots | The Journal of Physical Chemistry C, https://pubs.acs.org/doi/full/10.1021/acs.jpcc.1c05371, (accessed December 15, 2024).
13 *Colloids and Surfaces A: Physicochemical and Engineering Aspects*, 2023, **674**, 131946.
14 G. E. Cragg and A. L. Efros, *Nano Lett.*, 2010, **10**, 313–317.
15 C. Melnychuk and P. Guyot-Sionnest, *J. Phys. Chem. Lett.*, 2018, **9**, 2208–2211.
16 J. Liu, P. Liu, T. Shi, M. Ke, K. Xiong, Y. Liu, L. Chen, L. Zhang, X. Liang, H. Li, S. Lu, X. Lan, G. Niu, J. Zhang, P. Fei, L. Gao and J. Tang, *Nat Commun*, 2023, **14**, 5352.
17 S. Zhang, C. Bi, Y. Tan, Y. Luo, Y. Liu, J. Cao, M. Chen, Q. Hao and X. Tang, *ACS Nano*, 2022, **16**, 18822–18829.
18 T. H. Dang, M. Cavallo, A. Khalili, E. Bossavit, H. Zhang, Y. Prado, C. Abadie, E. Dandeu, S. Ithurria, G. Vincent, Y. Todorov, C. Sirtori, A. Vasanelli and E. Lhuillier, *ACS Photonics*, 2024, **11**, 1928–1934.
19 H. Zhang, Y. Prado, R. Alchaar, H. Lehouelleur, M. Cavallo, T. H. Dang, A. Khalili, E. Bossavit, C. Dabard, N. Ledos, M. G. Silly, A. Madouri, D. Fournier, J. K. Utterback, D. Pierucci, V. Parahyba, P. Potet, D. Darson, S. Ithurria, Bartłomiej Szafran, B. T. Diroll, J. I. Climente and E. Lhuillier, *Nano Lett.*, 2024, **24**, 5039–5046.
20 R. C. Keitel, M. C. Weidman and W. A. Tisdale, *J. Phys. Chem. C*, 2016, **120**, 20341–20349.
21 R. A. Maniyara, C. Graham, B. Paulillo, Y. Bi, Y. Chen, G. Herranz, D. E. Baker, P. Mazumder, G. Konstantatos and V. Pruneri, *APL Materials*, 2021, **9**, 021121.
22 R. Alchaar, C. Dabard, D. Mastrippolito, E. Bossavit, T. H. Dang, M. Cavallo, A. Khalili, H. Zhang, L. Domenach, N. Ledos, Y. Prado, D. Troadec, J. Dai, M. Tallarida, F. Bisti, F. Cadiz, G. Patriarche, J. Avila, E. Lhuillier and D. Pierucci, *J. Phys. Chem. C*, 2023, **127**, 12218.
23 M. Chen, X. Xue, T. Qin, C. Wen, Q. Hao and X. Tang, *Adv. Mater. Technol*, 2023, **8**, 2300315.
24 *Matter*, 2021, **4**, 3549–3584.
25 *Thin Solid Films*, 2010, **518**, 3075–3080.
26 F. G. Micallef, P. K. Shrestha, D. Chu, K. McEwan, G. Rughoobur, T. Carey, N. Coburn, F. Torrisi, O. Txoperena and A. Zurutuza, *Thin Solid Films*, 2018, **660**, 411.
27 C. Lee, J. Y. Kim, S. Bae, K. S. Kim, B. H. Hong and E. J. Choi, *Appl. Phys. Lett*, 2011, **98**, 071905.
28 C.-C. Lin, D.-Y. Wang, K.-H. Tu, Y.-T. Jiang, M.-H. Hsieh, C.-C. Chen and C.-W. Chen, *Appl. Phys. Lett*, 2011, **98**, 263509.
29 X. Tang, M. Chen, A. Kamath, M. M. Ackerman and P. Guyot-Sionnest, *ACS Photonics*, 2020, **7**, 1117.
30 C. Gréboval, U. N. Noumbé, A. Chu, Y. Prado, A. Khalili, C. Dabard, T. H. Dang, S. Colis, J. Chaste, A. Ouerghi, J.-F. Dayen and E. Lhuillier, *Appl. Phys. Lett*, 2020, **117**, 251104.
31 A. Chatterjee, N. B. Pendyala, A. J. K. S. R. K. Rao, and e-J., *Nanotechnol*, 2019, **17**, 95.
32 X. Tang, M. M. Ackerman, M. Chen and P. Guyot-Sionnest, *Nat. Photonics*, 2019, **13**, 277–282.
33 K. A. Sergeeva, H. Zhang, A. S. Portniagin, E. Bossavit, G. Mu, S. V. Kershaw, S. Ithurria, P. Guyot-Sionnest, S. Keuleyan, C. Delerue, X. Tang, A. L. Rogach and E. Lhuillier, *Advanced Functional Materials*, 2024, **34**, 2405307.

34 Y. Wang, L. Peng, J. Schreier, Y. Bi, A. Black, A. Malla, S. Goossens and G. Konstantatos, *Nat. Photon.*, 2024, **18**, 236–242.
35 M. M. Ackerman, *Information Display*, 2020, **36**, 19–23.
36 Y. Ding, S. Xiong, L. Sun, Y. Wang, Y. Zhou, Y. Li, J. Peng, K. Fukuda, T. Someya, R. Liu and X. Zhang, *Chem. Soc. Rev.*, 2024, **53**, 7784–7827.
37 L. Hu, H. S. Kim, J.-Y. Lee, P. Peumans and Y. Cui, *ACS Nano*, 2010, **4**, 2955.
38 R. Zhang and M. Engholm, *Nanomaterials*, 2018, **8**, 628.
39 J.-Y. Lee, S. T. Connor, Y. Cui and P. Peumans, *Nano Lett.*, 2008, **8**, 689–692.
40 R. Xu, S. Ruan, D. Zhang, Z. Li, B. Yin, K. Li, J. Zhou, Y. Chen and C. Li, *Journal of Alloys and Compounds*, 2018, **751**, 117–123.
41 N. Cui, Y. Song, C.-H. Tan, K. Zhang, X. Yang, S. Dong, B. Xie and F. Huang, *npj Flex Electron*, 2021, **5**, 1–8.
42 P. Jing, W. Ji, Q. Zeng, D. Li, S. Qu, J. Wang and D. Zhang, *Sci Rep*, 2015, **5**, 12499.
43 S. Kim, J. Kim, D. Kim, B. Kim, H. Chae, H. Yi and B. Hwang, *ACS Appl. Mater. Interfaces*, 2019, **11**, 26333–26338.
44 L. Meng, M. Zhang, H. Deng, B. Xu, H. Wang, Y. Wang, L. Jiang and H. Liu, *CCS Chemistry*, 2020, **3**, 2194–2202.
45 X.-Y. Zeng, Q.-K. Zhang, R.-M. Yu and C.-Z. Lu, *Advanced Materials*, 2010, **22**, 4484–4488.
46 S. Devaraju, A. K. Mohanty, D. Won and H. Paik, *Mater. Adv.*, 2023, **4**, 1769–1776.
47 W. Lan, Y. Chen, Z. Yang, W. Han, J. Zhou, Y. Zhang, J. Wang, G. Tang, Y. Wei, W. Dou, Q. Su and E. Xie, *ACS Appl. Mater. Interfaces*, 2017, **9**, 6644.
48 J. Kim, E. K. Ampadu, W. J. Choi and E. Oh, *Nanotechnology*, 2019, **30**, 075201.
49 K. A. Son, D. Wong, H. Sharifi, H. C. Seo, T. D. Lyon, S. Terterian, J. S. Moon and T. Hussain, *IEEE Trans. Nanotechnol*, 2015, **14**, 10.
50 E. W. Malachosky, M. M. Ackerman and L. Stan, *Nanomaterials (Basel)*, 2024, **14**, 1354.
51 M. Yu, B. Wang, R. Huang, H. Xia, J. Liu, C. Deng, J. Zhang, L. Gao, J. Tang and X. Lan, *ACS Photonics*, DOI:10.1021/acsphotonics.4c00911.
52 M. M. Ackerman, M. Chen and P. Guyot-Sionnest, *Applied Physics Letters*, 2020, **116**, 083502.
53 J. Yang, H. Hu, Y. Lv, M. Yuan, B. Wang, Z. He, S. Chen, Y. Wang, Z. Hu, M. Yu, X. Zhang, J. He, J. Zhang, H. Liu, H.-Y. Hsu, J. Tang, H. Song and X. Lan, *Nano Lett.*, 2022, **22**, 3465–3472.
54 X. Shen, J. C. Peterson and P. Guyot-Sionnest, *ACS Nano*, 2022, **16**, 7301.
55 F. Lavini, A. Calò, Y. Gao, E. Albisetti, T.-D. Li, T. Cao, G. Li, L. Cao, C. Aruta and E. Riedo, *Nanoscale*, 2018, **10**, 8304.
56 M. M. Ackerman, X. Tang and P. Guyot-Sionnest, *ACS Nano*, 2018, **12**, 7264–7271.
57 C. Gréboval, E. Izquierdo, C. Abadie, A. Khalili, M. Cavallo, A. Chu, T. H. Dang, H. Zhang, X. Lafosse, M. Rosticher, X. Z. Xu, A. Descamps-Mandine, A. Ouerghi, M. G. Silly, S. Ithurria and E. Lhuillier, *ACS Appl. Nano Mater.*, 2022, **5**, 8602–8611.
58 A. Jagtap, N. Goubet, C. Livache, A. Chu, B. Martinez, C. Gréboval, J. Qu, E. Dandeu, L. Becerra, N. Witkowski, S. Ithurria, F. Mathevet, M. G. Silly, B. Dubertret and E. Lhuillier, *J. Phys. Chem. C*, 2018, **122**, 14979–14985.
59 X. He, R. He, A. Liu, X. Chen, Z. Zhao, S. Feng, N. Chen and M. Zhang, *J. Mater. Chem. C*, 2014, **2**, 9737.
60 H. Lu, J. Luo, Y. Liu, Y. Zhong, J. Wang and Y. Zhang, *IEEE J. Photovolt*, 2019, **9**, 710.
61 M. Chen, X. Xue, T. Qin, C. Wen, Q. Hao and X. Tang, *Advanced Materials Technologies*, 2023, **8**, 2300315.
62 J. Meng, J. A. Röhr, H. Wang, B. E. Sartor, D. Song, A. Katzenberg, M. A. Modestino, Z. Xu, J. Kong and A. D. Taylor, *Solar RRL*, 2022, **6**, 2100794.
63 S. B. Hafiz, M. M. A. Mahfuz and D.-K. Ko, *ACS Appl. Mater. Interfaces*, 2021, **13**, 937.
64 A. Rogalski, J. Mikołajczyk, J. Wojtas, M. Kopytko, K. Achtenberg and Z. Bielecki, *Bulletin of the Polish Academy of Sciences Technical Sciences; 2022; 70; 2; e140534*.
65 A. Rogalski, *ACS Photonics*, 2023, **10**, 647–653.
66 R. Saran and R. J. Curry, *Nat. Photon*, 2016, **10**, 81.
67 B. Wang, M. Yuan, J. Liu, X. Zhang, J. Liu, J. Yang, L. Gao, J. Zhang, J. Tang and X. Lan, *Nano Lett.*, 2024, **24**, 9583–9590.

Data availability

Additional data supporting this article have been included as part of the Supplementary Information. Further data from the main text and supplementary information are provided on the open science framework platform at the link: https://osf.io/ye2as/?view_only=48621a03661b4abfb502ed3fd5bf2d92